Effects of Slot Injection on Detonation Wavelet Characteristics in a Rotating Detonation Engine

Chian Yan [1*], Honghui Teng [2] and Hoi Dick Ng [1]

[1] Department of Mechanical, Industrial and Aerospace Engineering, Concordia University, Montreal, QC H3G 1M8, Canada
[2] School of Aerospace Engineering, Beijing Institute of Technology, Beijing 100081, China

*** Correspondence:** chian.yan@concordia.ca

Highlights

(maximum 85 characters, including spaces, per bullet point)

- The detonation wavelets with slot injections are resolved computationally with GPU.
- Flow features are compared between the slot injection and micro-nozzle injection.
- The wavelet number dependence on slot injection stagnation properties are studied.
- The instabilities induced by the slot injections in rotating detonation are highlighted.

Effects of Slot Injection on Detonation Wavelet Characteristics in a Rotating Detonation Engine

Chian Yan [1*], Honghui Teng [2] and Hoi Dick Ng [1]

[1] Department of Mechanical, Industrial and Aerospace Engineering, Concordia University, Montreal, QC H3G 1M8, Canada

[2] School of Aerospace Engineering, Beijing Institute of Technology, Beijing 100081, China

* Correspondence: chian.yan@concordia.ca

Abstract

Two-dimensional numerical simulations are performed to investigate the effects of spatially discrete slot injection of reactants on the features of detonation wavelets in a rotating detonation engine (RDE). The detonation dynamics is described by a model based on the reactive Euler equations coupled with two-step, induction-reaction kinetics. By varying injection conditions and the chemical sensitivity of the reactive mixture, a parametric study is carried out to examine the influence of the injection-slot area ratio α on the detonation wavelet patterns and different flow features inside an RDE combustion chamber. The simulation results demonstrate that the injection conditions, i.e., stagnation temperature and pressure, have a similar influence on slot-nozzle rotating detonation wavelets (RDWs) as compared with the mini-nozzle RDWs reported in a previous study. The corresponding mass flow rate and inhomogeneity generated due to the presence of slot injection, however, play a key factor in the self-sustained rotating detonation and its frontal structure.

Keywords: Detonation; rotating detonation engines; slot injection; two-step kinetics

1. Introduction

In recent years, detonative combustion has attracted renewed interest in propulsion applications [1, 2]. As a form of pressure-gain combustion, it provides a potential improvement in the thermal efficiency of propulsion-related engine systems. In addition, the detonation-based engine components are much simpler as compared to conventional deflagrative gas turbine engines. The concept of utilizing detonation for propulsion has indeed been considered in many supersonic combustion applications including, most notably, ram accelerators [3], oblique detonation wave engines (ODWEs) [1, 4], and pulse-detonation engines (PDEs) [5, 6]. Recently, the main focus of detonation-based engine technology has shifted towards another novel variant – Rotating Detonation Engine (RDE) [7-13] (as illustrated in Fig. 1). The basic concept of an RDE exploits continuous detonation propagation around a thin annular channel combustor with side relief as the flow expands towards the nozzle, generating the engine thrust. The continuous detonation mode permits an RDE to operate at a higher frequency with a reduced mechanical complexity and stably produce a continuous thrust. The flexibility of RDE combustors also provides a promising route to its integration into a high-speed airbreathing engine or rocket system.

In a typical RDE, premixed reactants are fed axially into the annular chamber from one end of the RDE. In general, the combustion field in an RDE chamber consists of a detonation consuming the injected reactants, an induced oblique shock, a contact surface, and an unstable slip line due to the Kelvin-Helmholtz instability. This shock-reaction wave complex is often referred to as a *rotating detonation wavelet* (RDW). Wave and combustion dynamics of an RDE such as the formation, stability, and characteristics of the wavelet structure have been investigated through a wealth of experiments and numerical simulations. Depending on the reactant properties, injection conditions, and geometric characteristics of the annular combustor, one or multiple detonation

wavelets can spin in the annular combustor. The propagation mode of these wavelets could also be unsteady – shifting instantaneously from one pattern to another, under some conditions, in a chaotic fashion – as observed in both experimental and numerical results [14-33]. The propulsive performance of RDEs has also been evaluated in some previous studies [34-41]. More comprehensive, detailed reviews of the recent advance in RDE research and development can be found in Refs. [7-13].

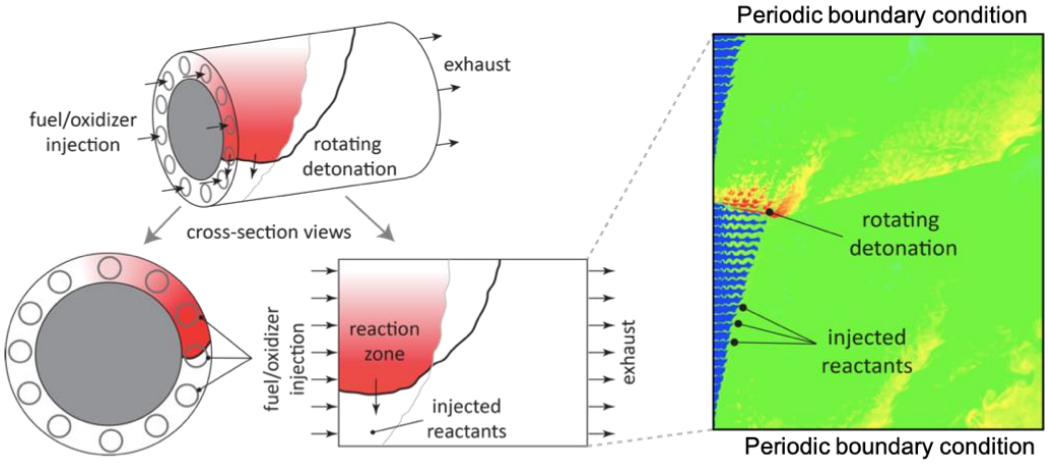

Figure 1. A schematic of the rotating detonation engines and a two-dimensional unwrapped computational domain

Although a substantial collection of RDW propagation modes has been observed previously in experiments and numerical simulations, the detailed mechanisms giving rise to different propagation modes and instabilities still elude the researchers. Among a large set of contributing factors, the current paper reports a computational study examining the effects of reactant injection conditions on the formation and persistence of RDW propagation modes. To model the flow field inside an RDE, the canonical setup considers a simplified, unwrapped two-dimensional geometry of an annular combustor wherein the flow variation in the radial direction is neglected. Such configuration is often valid for the cases that the annular width of the RDE combustion chamber is much smaller than its azimuthal and axial lengths. In this simplified representation, the injection

can be incorporated as boundary conditions of the computational domain where each edge grid point is modeled as a micro-nozzle (as illustrated in Fig. 2(b)). Different parameters, such as the inlet pressure, Mach number, micro-nozzle area ratio, are related through the quasi-one-dimensional gas dynamics relations, determining the inflow conditions across the injection boundary at each time step. A more realistic approach to model the process is to consider spatially discrete slot injectors, e.g., those in Ref. [42-44]. In fact, these studies show that the rotating detonation is very sensitive to how the injection is modeled – from an idealized representation of micro-nozzles to actually modeling individual slot injectors. By considering slot injectors, it introduces another important geometric parameter, i.e., slot area ratio, which in turn controls the mass flow rate into the rotating detonation engine chamber. The flow disturbance induced by individual slot jets could also affect the stable propagation of the rotating detonation.

In this work, using numerical simulations, we attempt to correlate the multiple detonation wavelet formations with a focus on the slot injection characteristics. In particular, this study aims to compare the results from Ref. [45] where micro-nozzle approximation was invoked and pinpoint the influence of discrete injection slots with a finite spacing between each two neighboring slots. A simplified two-step, induction-reaction kinetic model is used with parameters calibrated against the steady-state detonation properties calculated using the detailed chemical kinetics of a stoichiometric hydrogen-air mixture again at initial conditions corresponding to a flight altitude of 18 km with (p_o = 7565.2 Pa and T = 216.7 K) [45]. This simplification in chemical kinetics permits one to perform high-resolution simulations of detonation phenomena at a reduced computational cost. The two-step, induction-reaction kinetic model has been demonstrated to adequately capture the salient features of gaseous detonation dynamics. The formation and instabilities of RDWs

resulting from the simulations are analyzed. The dependence of RDW propagation on the injection parameters is discussed.

The paper is organized as follows: In § 2, the physical geometry, the ideal detonation model by the two-dimensional reactive Euler equations with a two-step induction-reaction kinetics, basic gas dynamic injection nozzle relationships, and the numerical method for solving the governing equations are described. § 3 reports the results of the resolution study and introduce the way to obtain the mass flow rate from the simulation data. In § 4, simulation results are presented and the flow features induced by discrete injection ports are discussed. The dependence on the wavelet patterns on different chemical and injection parameters are examined. § 5 concludes the paper.

2. Computational Setup

For the unwrapped two-dimensional RDE, the ideal detonation flow model is given by the ideal reactive Euler equations:

$$\frac{\partial U}{\partial t}+\frac{\partial F}{\partial x}+\frac{\partial G}{\partial y}=S \tag{1}$$

$$U=\begin{bmatrix}\rho\\ \rho u\\ \rho v\\ \rho e\\ \rho\xi\\ \rho\lambda\end{bmatrix}, F=\begin{bmatrix}\rho u\\ \rho u^2+p\\ \rho uv\\ \rho u(e+p)\\ \rho u\xi\\ \rho u\lambda\end{bmatrix}, G=\begin{bmatrix}\rho v\\ \rho uv\\ \rho v^2+p\\ \rho v(e+p)\\ \rho v\xi\\ \rho v\lambda\end{bmatrix}, S=\begin{bmatrix}0\\ 0\\ 0\\ 0\\ \dot{\omega}_{\mathrm{I}}\\ \dot{\omega}_{\mathrm{R}}\end{bmatrix}, \tag{2}$$

with

$$e=\frac{p}{(\gamma-1)\rho}+\frac{1}{2}(u^2+v^2)-\lambda Q, \tag{3}$$

$$p=\rho T \tag{4}$$

The source terms are described by a two-step induction-reaction kinetic model [46] which is previously used in a number of previous detonation studies, e.g., [45, 47-52].

$$\dot{\omega}_{\mathrm{I}}=H(1-\xi)\rho k_{\mathrm{I}} exp\left[E_{\mathrm{I}}\left(\frac{1}{T_{\mathrm{S}}}-\frac{1}{T}\right)\right], \tag{5}$$

$$\dot{\omega}_{\mathrm{R}} = [1 - H(1-\xi)]\rho(1-\lambda)k_{\mathrm{R}} exp\left[\left(-\frac{E_{\mathrm{R}}}{T}\right)\right], \tag{6}$$

where E_{R} is the activation energy of heat release, E_{I} is the activation energy of induction, and the Heaviside step function H is given by:

$$H(1-\xi) = \begin{cases} 1, & \xi \leq 1, \\ 0, & \xi > 1. \end{cases} \tag{7}$$

All the flow variables have been made dimensionless by reference to the uniform unburned state:

$$\rho = \frac{\tilde{\rho}}{\tilde{\rho}_0}, p = \frac{\tilde{p}}{\tilde{p}_0}, T = \frac{\tilde{T}}{\tilde{T}_0}, u = \frac{\tilde{u}}{\sqrt{\tilde{R}\tilde{T}_0}}, v = \frac{\tilde{v}}{\sqrt{\tilde{R}\tilde{T}_0}}, Q = \frac{\tilde{Q}}{\tilde{R}\tilde{T}_0}, E_a = \frac{\tilde{E}_{\mathrm{a}}}{\tilde{R}\tilde{T}_0}. \tag{8}$$

The variables ρ, u, v, p, e, and Q are the density, velocities in *x*- and *y*- direction, pressure, total energy, and the amount of chemical heat release, respectively. The pre-exponential factor k_{I} of the induction step is chosen to define the spatial reference scale, so the induction length is unit, i.e., $\Delta_{\mathrm{I}} = 1$ or $k_{\mathrm{I}} = -u_{\mathrm{vn}}$. In this study, the dimensionless thermodynamic parameters of the combustible mixture are $Q/RT_{\mathrm{o}} = 25.31$, $\gamma = 1.32$, $\varepsilon_{\mathrm{I}} = 6.52$, $\varepsilon_{\mathrm{R}} = 1.0$, $k_{\mathrm{I}} = 1.0538$, $k_{\mathrm{R}} = 3.74$, $T_{\mathrm{s}}/T_{\mathrm{o}} = 5.830$ and $M_{\mathrm{CJ}} = 5.54$. These properties correspond approximately to a stoichiometric hydrogen/oxygen mixture at 7565.2 Pa and 216.7 K corresponding to a flight altitude of 18 km [45].

The solutions to the governing equation system are obtained numerically using a 2nd order MUSCL-Hancock scheme with an HLLC Riemann solver [53], with a CFL number of 0.90. To accelerate the simulations, the entire flow solver [54-56] was implemented taking advantage of parallel computing enabled by an Nvidia Tesla K40 graphics processing unit (GPU). In this work, the default resolution considered is 16 pts per induction zone length Δ_{I}.

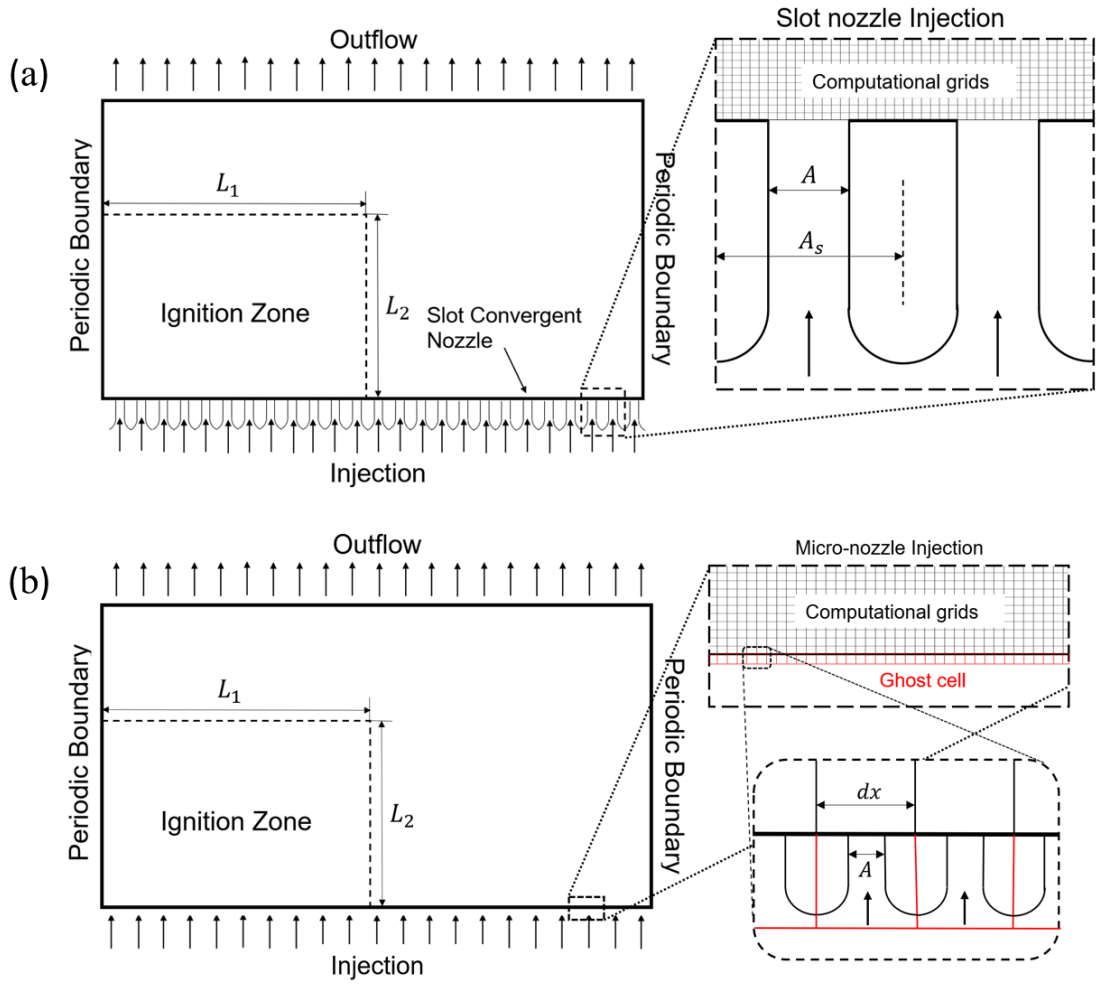

Figure 2. Schematic of the computational domain and the initiation of detonation waves of (a) slot nozzle injection and a zoom-in geometry of the nozzle structure; (b) micro-nozzle injection and a double zoom-in of the micro-nozzles in computational grid points

The computational domain and a sketch of the injection slot nozzle arrangement are shown in Fig. 2(a). The left and right boundaries are modeled by periodic boundary conditions. The top is the engine outlet described by a transmission boundary. The bottom is an inflow plane with multiple convergent slot nozzles injecting combustible mixture. The injection area ratio $\alpha = A/A_s$ refers to the area of a slot nozzle throat over the area of a slot unit, as shown in Fig. 2(a). In a macroscopic way, this area ratio α also refers to the sum of the throat area of all slot nozzles over the total bottom boundary area of the combustion chamber. The walls between each slot nozzle

are set as reflective boundary conditions, and the injection slot nozzles conditions in each grid point are described by the following:

(i) For $p \geq p_0$, there is no injection flow and the boundary is considered as a reflective boundary condition;

(ii) For $p_0 \geq p \geq P_{\mathrm{cr}}$, the convergent nozzle is not choked:

$$p_i = p,\ T_i = T_0\left(\frac{p_i}{p_0}\right)^{\frac{\gamma-1}{\gamma}},\ u = 0, \text{and}\ v = \sqrt{\frac{2\gamma}{\gamma-1}T_0\left[1-\left(\frac{p_i}{p_0}\right)^{\frac{\gamma-1}{\gamma}}\right]} \tag{9}$$

(iii) For $p < p_{\mathrm{cr}}$, the convergent nozzle is choked and $p_i = p_{\mathrm{cr}}$. The temperature and velocity can be calculated by the expressions in part (2).

The critical pressure is defined by the stagnation pressure p_0 and the specific heat ratio γ:

$$p_{\mathrm{cr}} = p_0\left(\frac{2}{\gamma+1}\right)^{\frac{\gamma}{\gamma-1}} \tag{10}$$

In this computational setup, the grid points in slot nozzle throats are essentially considered as multiple independent micro-nozzles. In this study, the compressible flow in the nozzle simplified into a quasi 1-D gas dynamics problem. In a more proper way of modelling the injection, a two-dimensional flow in the nozzle should be considered.

Note that when the injection area ratio $\alpha = 1$, the walls between each slot are eliminated. In this case, the slot nozzle injection is equivalent to the micro-nozzle injection. Figure 2(b) shows the schematic of the micro-nozzle injection. As we have mentioned above, the injection is incorporated as boundary conditions of the computational domain where each edge grid point is modeled as a micro-nozzle. In the double zoom-in of Fig. 2(b), the micro-nozzles are aligned inside ghost cells along the bottom grid points and the length scale of a micro-nozzle unit is equal to the length of a computational grid point length. The area ratio of a micro-nozzle $\alpha = A/dx$ refers to the area of the micro-nozzle throat A over the computational grip size dx. When $\alpha < 1$, the micro-nozzle throat

area is less than the bottom area. When the slot area ratio $\alpha = 1$, the number of the micro-nozzles aligned along the bottom boundary equals the number of computational grids in the *x*-axis and the area ratio of these micro-nozzle also equals 1, thus the slot nozzle injection and the micro-nozzle injection can be considered equivalent.

The domain size is fixed at $L_x \times L_y = 400 \times 240$ and the ignition zone is set at $L_1 \times L_2 = 192 \times 150$. The ignition zone is a homogeneous high-pressure zone with $p_1 = 2p_{\mathrm{CJ}} = 35.5$ and $\rho_1 = \rho_{\mathrm{CJ}} = 1.715$. The initial pressure and density of the rest of the flow field in the computational domain are 1.0. It is observed that although all the RDWs in this study start with the same initial condition, the propagation direction of the RDW is rather unpredictable. Since the RDW is generated by the interaction and collisions between the left-going and right-going wavefronts crossing the periodic boundary, the direction of the leading detonation wave front differs randomly. In this study, the initial high-pressure ignition zone is stationary, and the left- and right-hand-side shocks of the ignition zone propagate simultaneously, and they are essentially equivalent. This makes propagation direction strongly unpredictable. However, after some numerical tests, we found that even imposing a fixed initial velocity u_x, the direction of the quasi-steady RDW is still random. For comparison, all the results shown in this study have been flipped as right-going RDWs. In this study, we focus on the general effect of slot nozzles on the established quasi-steady RDW structures rather than the initiation of RDW itself. In all the results shown in this paper, if not specified, the total number of the slot nozzles is equal to 40, and the default value of the stagnation pressure p_0 is 20 and the stagnation temperature T_0 is 4.0.

3. The Effect of Numerical Resolution and CFL number

A numerical resolution study is conducted to ensure results are not affected by different grid resolutions. In [45], it is proven that a grid of 5 pts/Δ_{I} is enough for the micro-nozzle injection

case. However, for the slot nozzle case, the injection of the combustible mixture is isolated from other slots. Stronger disturbance, more interactions, and finer details between nozzles, injection flows and detonation contact surfaces are introduced. Thus, a higher resolution is thus expected. In this part, finer grid scales of 10 pts/Δ_I, 16 pts/Δ_I, and 24 pts/Δ_I are considered for the resolution test study.

To quantitatively demonstrate grid convergence of the numerical results and subsequently analyze the effect of slot injection, we calculate from the numerical simulation data the total injection mass flow rate $\dot{m}$ given by:

$$\dot{m} = \sum_{i=1}^{L_x \times \alpha \times i_{L_i}} \rho_i v_i A' \tag{11}$$

where α is the slot area ratio A/A_s; i_{L_i} the number of cells per induction zone length; ρ_i the local density of cell at the throat; v_i the local velocity of cell at the throat; and A' the area of a single cell $A' = 1/i_{L_i}$. The total injection mass flow rate $\dot{m}$ physically denotes the sum of the mass flow rate from each slot nozzle. Here, instead of obtaining the mass flow rate from averaging the density and velocity of each nozzle, $\dot{m}$ is computed based on the cells on the injection boundary. In the simulation, $\dot{m}$ is time-dependent. When the RDW reaches a quasi-steady state, $\dot{m}$ is found to stay at a relatively steady value. Shown in Fig. 3 is the average $\dot{m}$-t plot at α = 0.60 obtained in 10 simulation repeats for the three grid resolutions. The trend of the three curves is the same and all approach to the same quasi-steady $\dot{m}$ value after t = 300. Due to the fact there is no significant discrepancy in terms of flow field features and mass flow rate value from the injection, to achieve a better computational time efficiency, the grid size of 16 pts/Δ_I is used as a default value for all subsequent simulations.

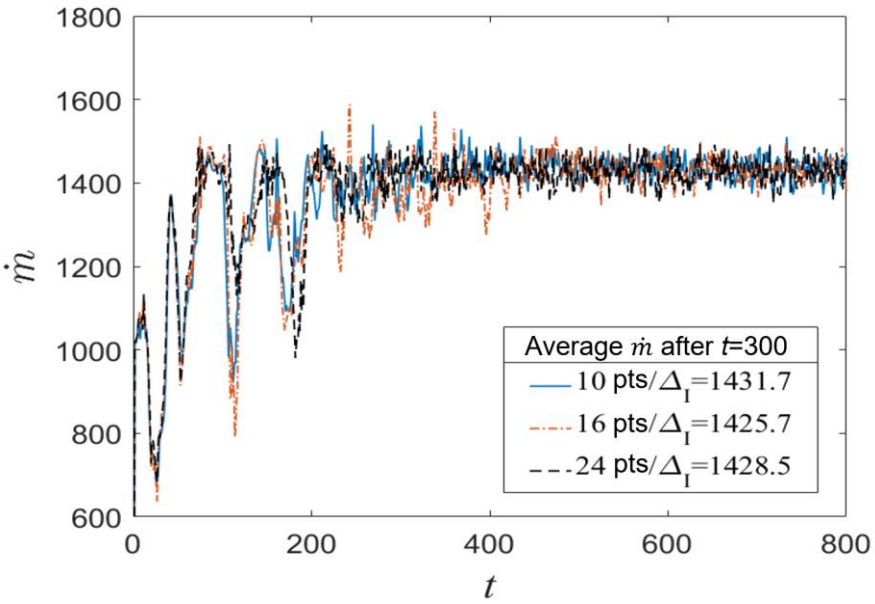

Figure 3. The mass flow rate evolution and the average $\dot{m}$ at α = 0.6 with 10 pts/Δ_I, 16 pts/Δ_I, and 24 pts/Δ_I

Figure 4 shows three contours of temperature field for a sample case with α = 0.60 at 10 pts/Δ_I, 16 pts/Δ_I, and 24 pts/Δ_I, respectively. All three resolutions show very similar flow structures of RDWs, such as the same number of wavelets, similar wavelet height, and contact surfaces. Due to the fact there is no significant discrepancy in terms of flow field features and mass flow rate value from the injection, to achieve a better computational time efficiency, the grid size of 16 pts/Δ_I is used as a default value for all subsequent simulations.

The essential characteristic of which the slot nozzle injection shows is that it brings a highly unstable inflow of unburnt combustible gas mixture into the chamber. Unlike the ideal micro-nozzle injection case where the detonation propagates into a more uniform injected mixture, the reactant in front of the detonation in the slot nozzles case is highly inhomogeneous. The strip-like fresh combustible injected and the Kelvin–Helmholtz (K-H) instability of the jets into the detonation products can be clearly seen from the temperature snapshot. Furthermore, the inhomogeneity generated by the slot nozzle influences the intrinsic cellular detonation stability,

resulting in a different unstable frontal structure of the rotating detonation as compared to the case with micro-nozzle [57]. The effect of inhomogeneity on the detonation wavelet pattern will be discussed later.

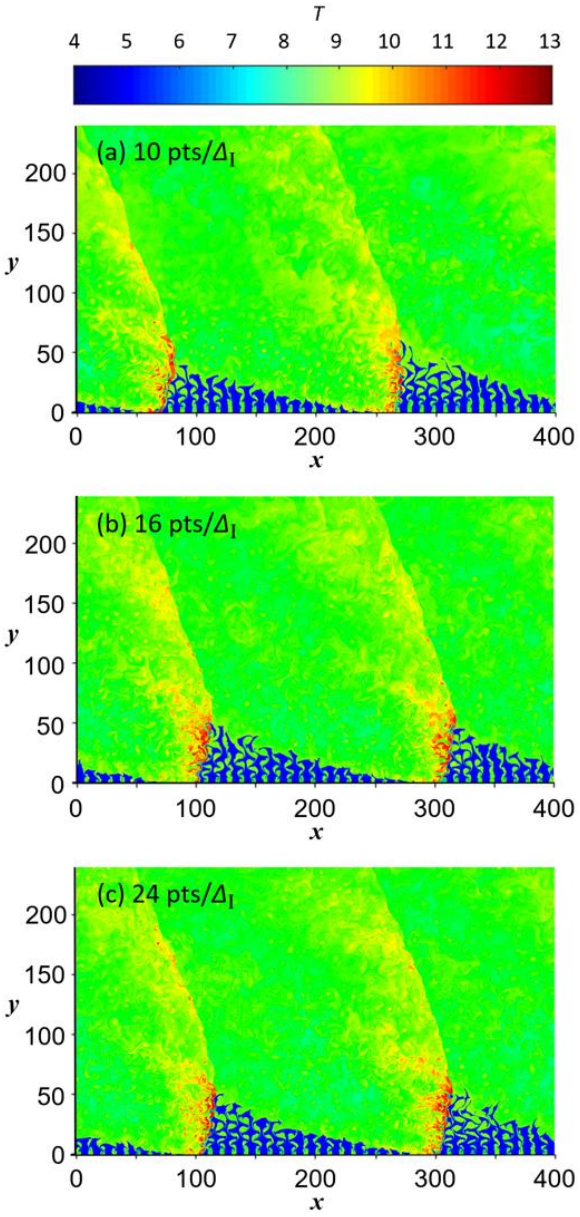

Figure 4. Temperature flow field of RDW at α = 0.6, (a) 10 pts/Δ_I; (b) 16 pts/Δ_I; and (c) 24 pts/Δ_I

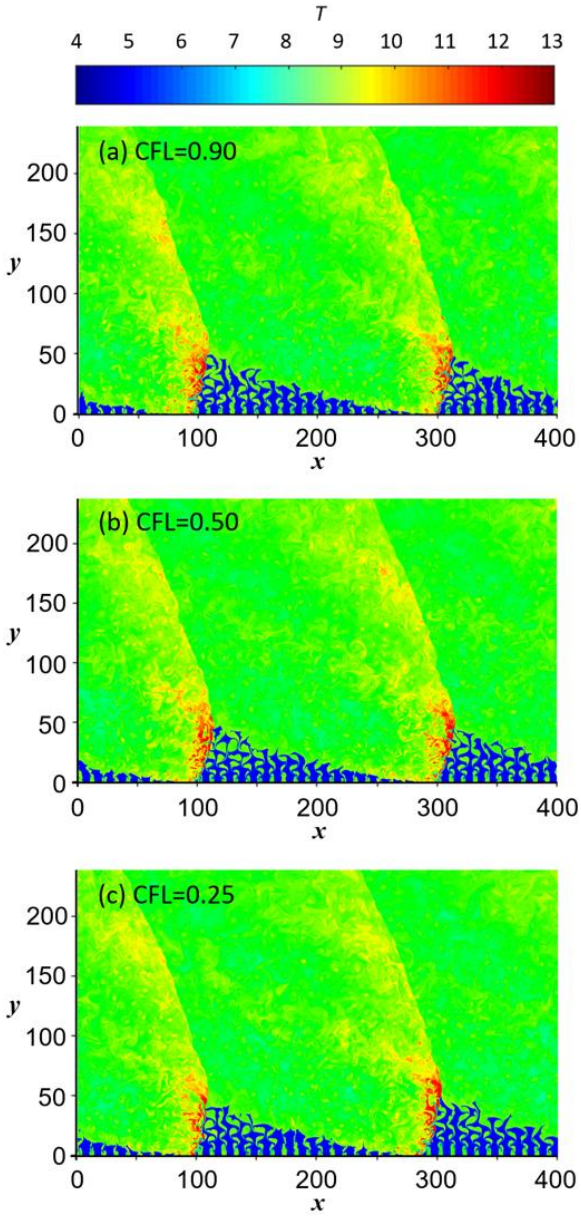

Figure 5. Temperature flow field of RDW at α = 0.6 with 16 pts/Δ_I and CFL number of (a) 0.90; (b) 0.50; (c) 0.25

Besides the numerical resolution study, the accumulation of errors from time-integration steps should be taken into consideration [58, 59]. Since that, it is necessary to verify the effect of time-step size. By reducing the Courant-Friedrichs-Lewy (CFL) number, numerical simulations with different sets of time steps are performed at α = 0.6 with 16 pts/Δ_I, see Fig. 5. The RDW structure, wavelet pattern, and injection process are not affected by the variation of CFL number. And also, the average total injection mass flow rates for the quasi-steady RDW are 1425.7, 1427.1 and 1430.3 for CFL number of 0.90, 0.50 and 0.25, respectively. Hence, the CFL number of 0.90 is selected as the default CFL number value.

4. Results and Discussion

4.1. Effect of slot nozzle area ratio, α

Figure 6 shows the temperature contours of different throat area ratios, α. In the first two cases where α = 0.3 and 0.4, the temperature contours reveal no steady RDW. The left- and right-going reactive fronts are colliding with each other but do not result in an RDW. For the case with α = 0.3 shown in Fig. 6, the pressure variation along the horizontal plane y = 25 is given in Fig. 7. The peak pressure is far below a typical RDE, for instance, α = 0.7, and the variation of pressure suggests the RDE extinction, despite there is some random local explosion within the flow. In fact, by further reducing α to 0.2, a similar wavelet pattern with more chaotic reactive fronts can be observed; when α = 0.1, the colliding waves cannot be seen anymore, and some random structures appear instead. From α = 0.5 to 0.9, RDWs at quasi-steady state induced by slot nozzle injection can be observed. When the nozzle area ratio α finally reaches 1.0, there is no slot anymore and the boundary condition is considered as an ideal micro-nozzle injection boundary condition. Apart from the failure situation, as the nozzle slot area ratio increases, the wave pattern turns to be more

and more stable. With increasing α, the mixture is becoming more homogeneous with less disturbance caused by the K-H instability from the slot injections. The contact surface behind the wavelet structure is more apparent for a more uniform reactant mixture with high α.

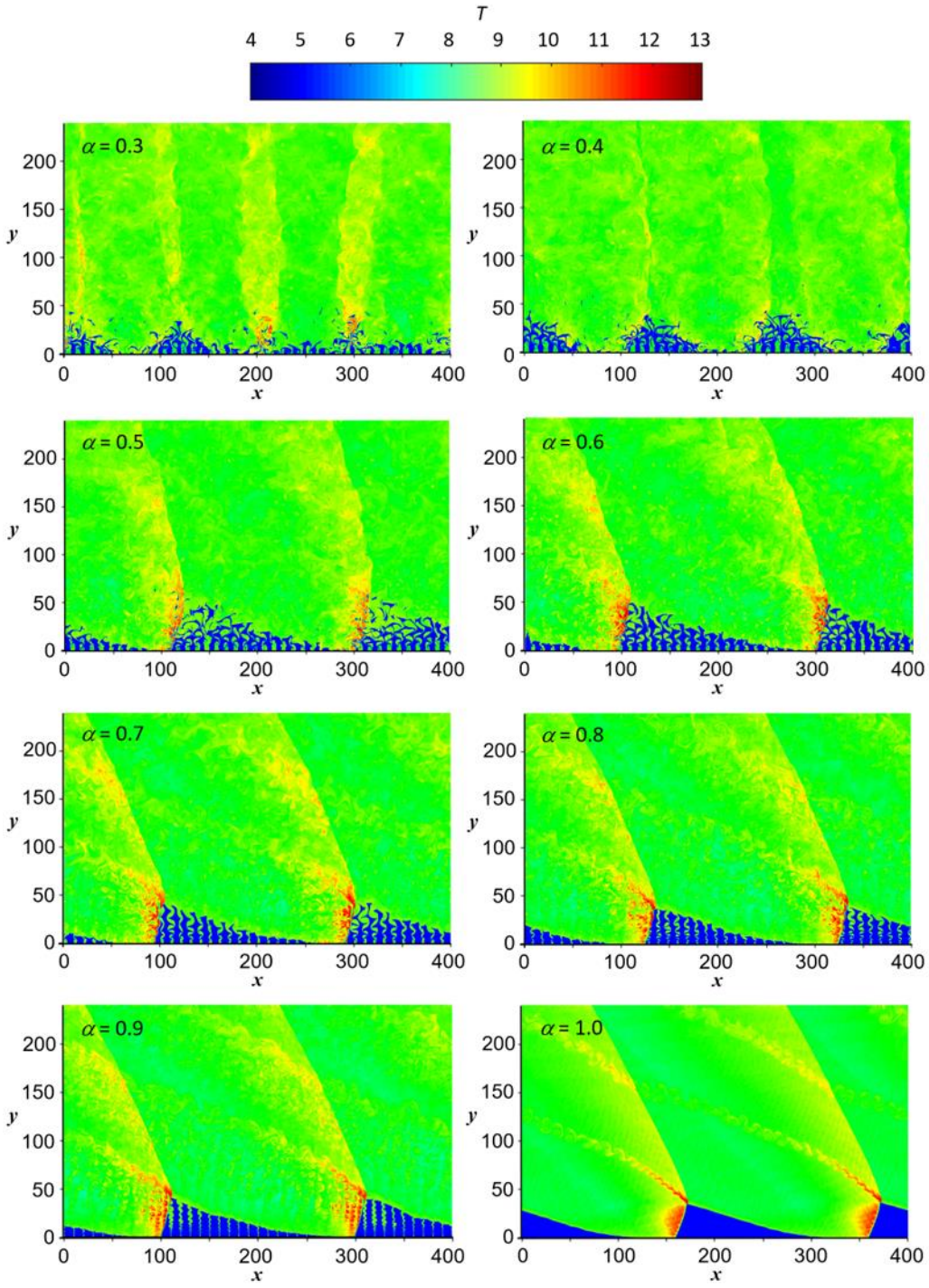

Figure 6. Temperature flow fields showing the effect of nozzle slot area ratio α from 0.3 to 1.0

As mentioned previously, Fig. 7 compares the pressure distribution along y = 25 horizontal plane of α = 0.3 and 0.7 at the frame shown in Fig. 6. It is clearly demonstrated that, with the disturbance of injection perturbation, the wave front pressure of α = 0.3 is essentially lower than that of α = 0.7. To further illustrate the wave pattern of α = 0.3, we focus on the y = 75 plane so that the pressure distribution shall not be significantly influenced by the injection.

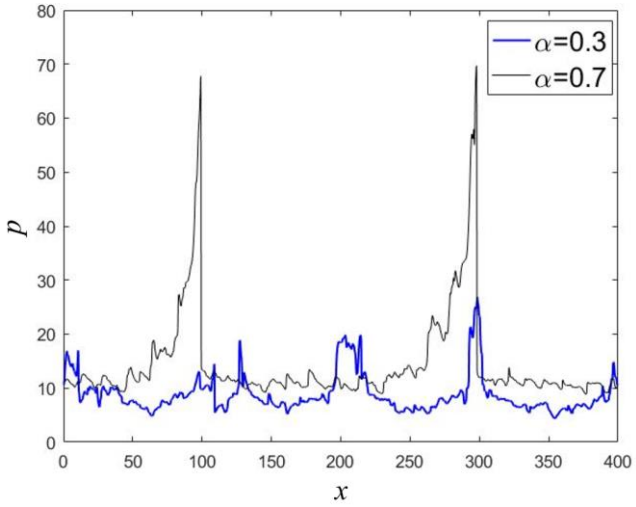

Figure 7. The pressure distribution along y = 25 for the case with α = 0.3 and 0.7

Figure 8 is the time-dependent pressure distribution along the horizontal plane y = 75. Compared with the regular 2-wavelet pattern RDW in α = 0.7, the relatively weak waves in α = 0.3 are colliding with each other periodically in contrast to a typical RDW pattern.

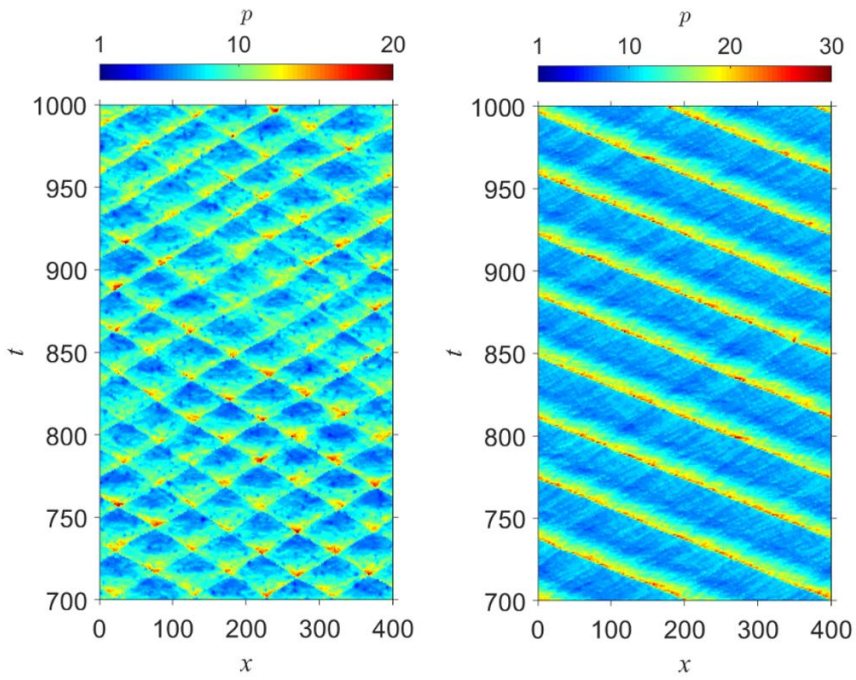

Figure 8. The time-dependent pressure along y = 75 plane for the case of α = 0.3 (left) and 0.7 (right)

The theoretical mass flow rate $\dot{m}_0$ is the mass flow rate when all the slot nozzles are choked and working at critical condition, which is defined by:

$$\dot{m}_0 = \rho_{\mathrm{cr}} v_{\mathrm{cr}}\, \alpha A \tag{12}$$

with ρ_{cr} the density of choked inflow and v_{cr} the velocity of choked inflow. The critical values are calculated by the relations describing the boundary condition provided in Sec. 2. Since in this study, the injection slot nozzle is the convergent nozzle, it is meaningful to compare the total mass flow rate $\dot{m}$ by numerical simulation with the theoretical mass flow rate $\dot{m}_0$ by gas dynamics. Table. 1 shows the comparison of the theoretical mass flow rate $\dot{m}_0$ and the average total mass flow rate $\dot{m}$. From the Table 1, it can be seen that along with the increasing nozzle slot area ratio and mass flow rate, the difference between numerical results and theoretical values are becoming larger. This means a larger number of nozzles are working at the non-choked condition. Thus, the injection efficiency does not rise proportionally to the enlargement of the injection area.

Table 1. Comparison of $\dot{m}_0$ and $\dot{m}$ at different throat area ratio

α	$\dot{m}_0$	$\dot{m}$	Difference
0.3	805.0	765.8	4.87%
0.4	1073.	992.8	7.51%
0.5	1341.7	1222.4	8.89%
0.6	1610.0	1425.7	11.50%
0.7	1878.	1579.2	15.92%
0.8	2146.7	1714.4	20.14%
0.9	2415.	1781.6	26.22%
1.0	2683.4	1852.6	30.96%

4.2 Effect of stagnation temperature and pressure on the wavelets formation

In [45], it is shown that for micro-nozzle injection, the number of wavelets is sensitive to the injection inflow stagnation temperature T_{st}. Even a slight change in stagnation temperature T_{st} can result in rapid transformation of wavelets. Generally, higher stagnation temperature T_{st} leads to a larger wavelet number. Figure 9 and Table 2 show the temperature contour and mass flow rate comparison for four different stagnation temperature cases at $\alpha = 0.6$.

Table 2. Comparison of $\dot{m}_0$ and $\dot{m}$ at various stagnation temperature

T_{st}	$\dot{m}_0$	$\dot{m}$	Difference
3.8	1681.9	1347.1	19.9%
4.0	1610.0	1425.7	11.5%
4.2	1571.2	1397.9	11.0%
4.3	1552.9	1367.5	11.9%

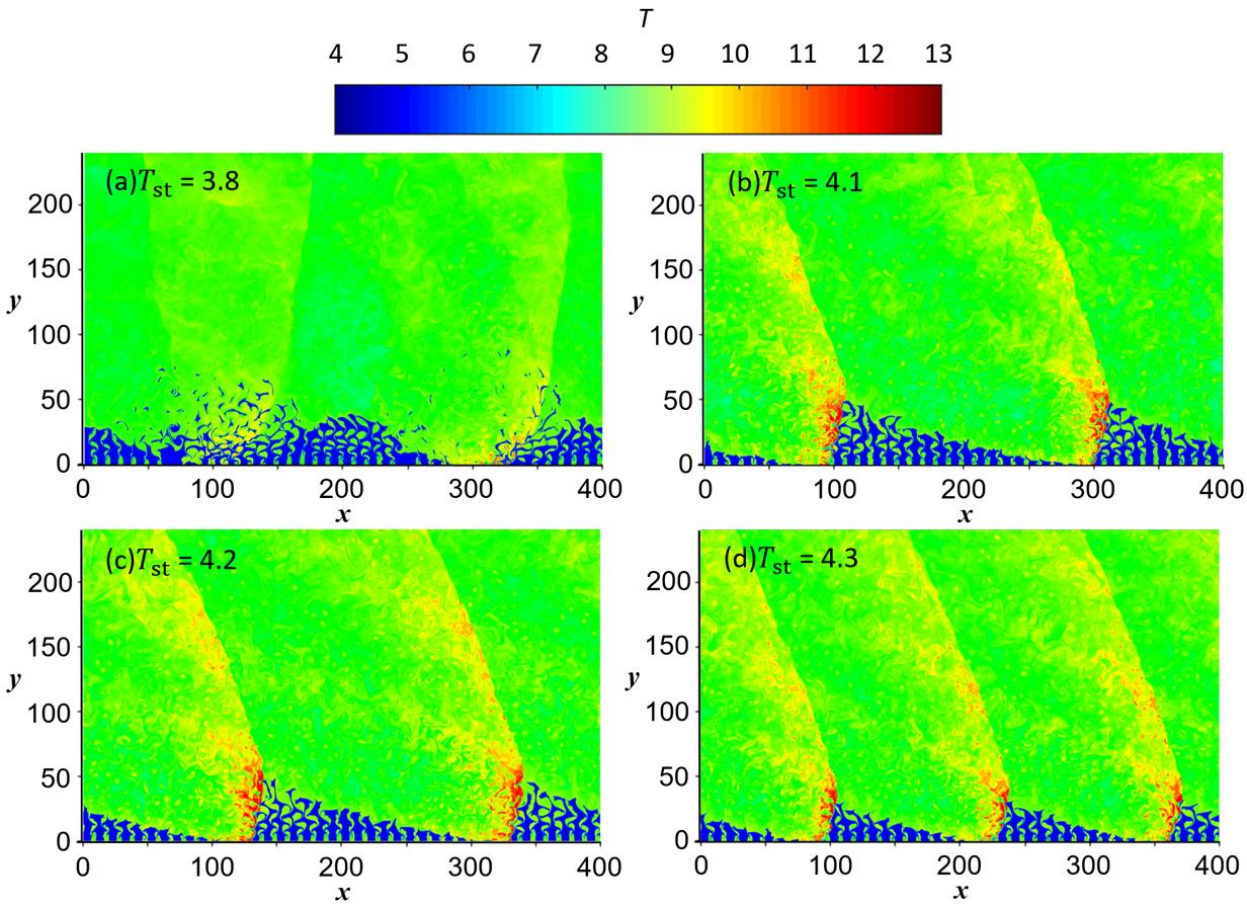

Figure 9. Temperature contour at α = 0.6, (a) T_{st} = 3.8; (b) T_{st} = 4.0; (c) T_{st} = 4.2; and (d) T_{st} = 4.3

At low stagnation temperature T_{st} = 3.8 shown in Fig. 9(a), though the rightward detonation waves have dominated the propagation, the RDW cannot be sustained stably. Furthermore, the difference between mass flow rates is higher than in the other three cases, resulting in the failure of quasi-steady RDW. Comparing the results between Fig. 9(c) T_{st} = 4.2 and Fig. 9(b) T_{st} = 4.0, we can see there is no significant change both in wave structures and mass flow rate. The wavelet number in slot nozzle injection is less sensitive to stagnation temperature than mini-nozzle. This could be a result of the less overall influence of inflow condition compared to mini-nozzle injection. For Fig. 9(d) T_{st} = 4.3, the wavelet mode comes a triple-wave operation. This is as expected from the previous study [45]. If we further increase the stagnation temperature, the

wavelet number could be dramatically enlarged. For example, when T_{st} = 5.0 (not shown here), the wavelet number could be as high as 7.

Inflow stagnation pressure P_{st} is another key factor influencing the injection process of the combustible mixture. In this study, the injection slot nozzle is the convergent nozzle. The effect of stagnation pressure in convergent nozzle flow is less critical than that in convergent-divergent nozzle flow. Only choked or non-choked boundary conditions are bonded with inflow. Since the injection density varies according to the change of stagnation pressure, the mass flow rate will also be affected. Figure 10 is the temperature contour at α = 0.6 and T_{st} = 4.0. Table 3 shows the numerical and theoretical mass flow rate under the corresponding conditions.

Table 3. Comparison of $\dot{m}_0$ and $\dot{m}$ at various stagnation pressure

P_{st}	$\dot{m}_0$	$\dot{m}$	Difference
10	805.0	662.6	17.7%
15	1207.5	1047.1	13.3%
20	1610.0	1397.9	11.0%
25	2012.6	1806.8	10.2%
30	2415.1	2143.9	11.2%

From the temperature contour shown in Fig. 10, we can see the wavelet number and the basic wave pattern do not vary very much. Though the stagnation pressure of Fig. 10(e) triples that of Fig. 10(a), the wavelet number is still 2. From Fig. 10(a) p_{st} = 10 to Fig. 10(c) p_{st} = 20, it appears that the rotating detonation wavelet height is becoming slightly larger but stays around 50 if stagnation pressure is over 20. Similarly, the mass flow rate data in Table 3 shows the difference between numerical results and theoretical results decreases when stagnation pressure increases from p_{st} = 10 to p_{st} = 40. The difference stops decreasing and stays relatively stable when stagnation pressure is over 20, which means the non-choked area of the wavelet front does not shrink when the stagnation pressure or the mass flow rate reaches a certain value.

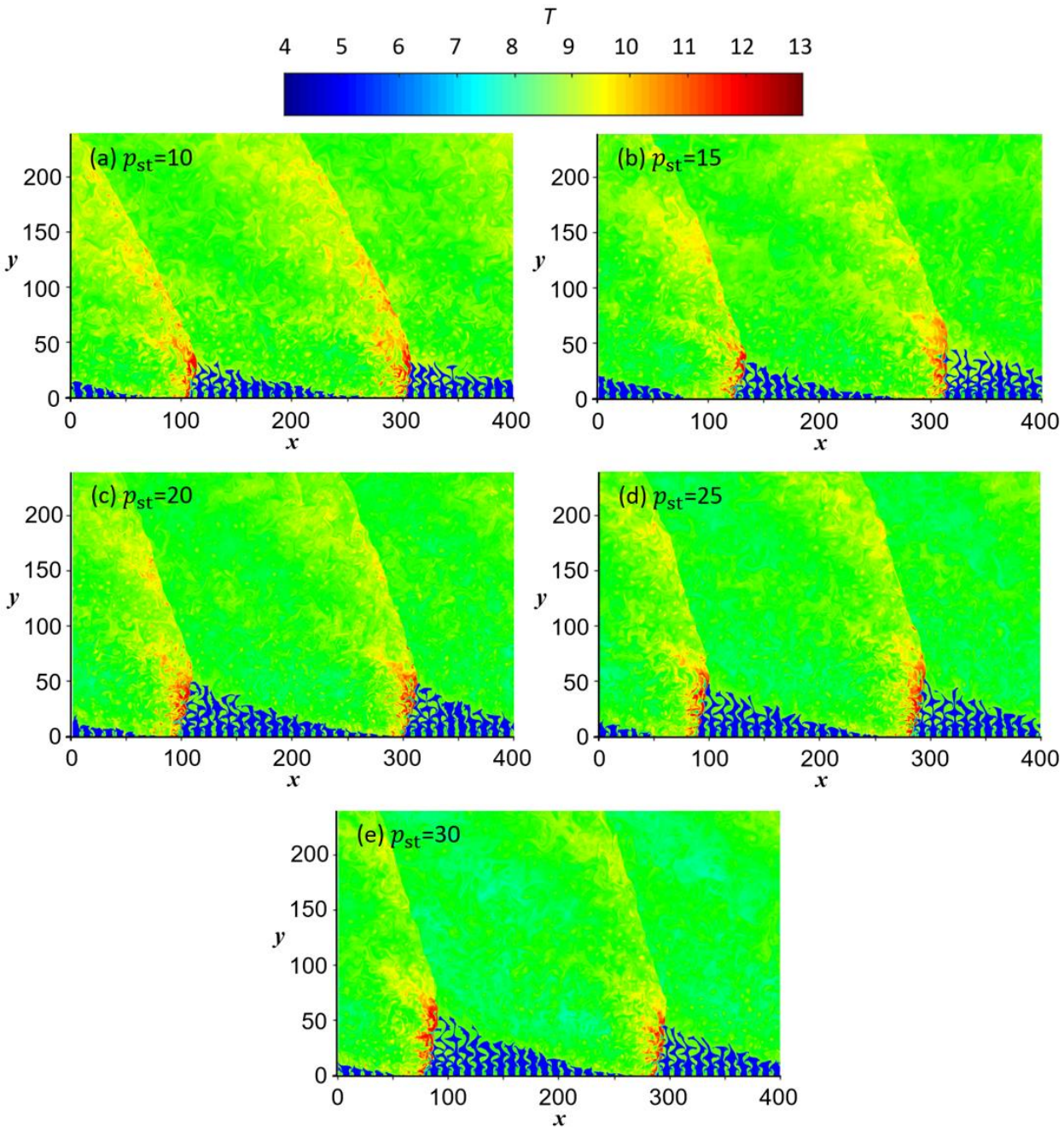

Figure 10. Temperature contour at α = 0.6, T_{st} = 4.0, (a) p_{st} = 10, (b) p_{st} = 15, (c) p_{st} = 20, (d) p_{st} = 25, and (e) p_{st} = 30

The mechanism is that in particularly low-pressure case like Fig.10(a) and Fig.10(b), the stagnation pressure is less than the Chapman-Jouguet pressure p_{CJ} = 17.75. The combustible pre-mixture injected into the combustion chamber is over-expanded. And in even lower stagnation cases like

p_{st} equal to 5, a steady RDW can no longer be maintained due to the lack of fuel. A second accelerate stage exists after the injection of the nozzle. This means the jet flow may not reach the maximum vertical velocity before the arrival of the detonation front, resulting in a lower wavelet height and higher non-choked area. Though the variation of injection stagnation pressure does influence mass flow rate significantly even in convergent nozzle setup, it is not the dominant factor that changes the number of wavelets and the injection efficiency when stagnation pressure is not low enough.

4.3 Effect of intrinsic chemical instability vs. injection instability

In the above sections, the chemical parameters for two-step kinetics modeling are selected corresponding to a designated flight altitude of 18 km. Here, various combustible fuel mixtures are considered by varying the pre-exponential factor k_R for the reaction process which controls the heat release rate, resulting in controlling the detonation reaction zone length. In previous numerical investigations [60], increasing $k_{R,}$ hence shortening the heat release pulse, can cause the detonation wave to become more unstable. For the RDE simulation with micro-nozzles, [45] shows that a decrease of k_R leads to a possibility of lower wavelet numbers, weaker K-H instability, smoother detonation wavefront, and the disappearance of transverse waves.

In this study, the effect of heat release rate k_R is also worthwhile to investigate for slot nozzles configuration. Figure 11 shows the temperature contours of RDW at T_{st} = 4.0. In Figs. 11(a)-(c), the slot nozzle area ratio α is 0.6. With the decrease of k_R, the temperature fluctuation behind the detonation front is weaker with the instability fading away. From the definition of the present two-step chemical kinetics model and basic features of an ideal steady ZND detonation structure, a decrease in k_R prolongs the length of the heat release region. According to the recent detonation stability theory [60], a broader heat release zone, or energy release pulse, has a benefit to sustain

the coherence of energy release and is less sensitive to flow disturbance, giving a more stable detonation wave propagation.

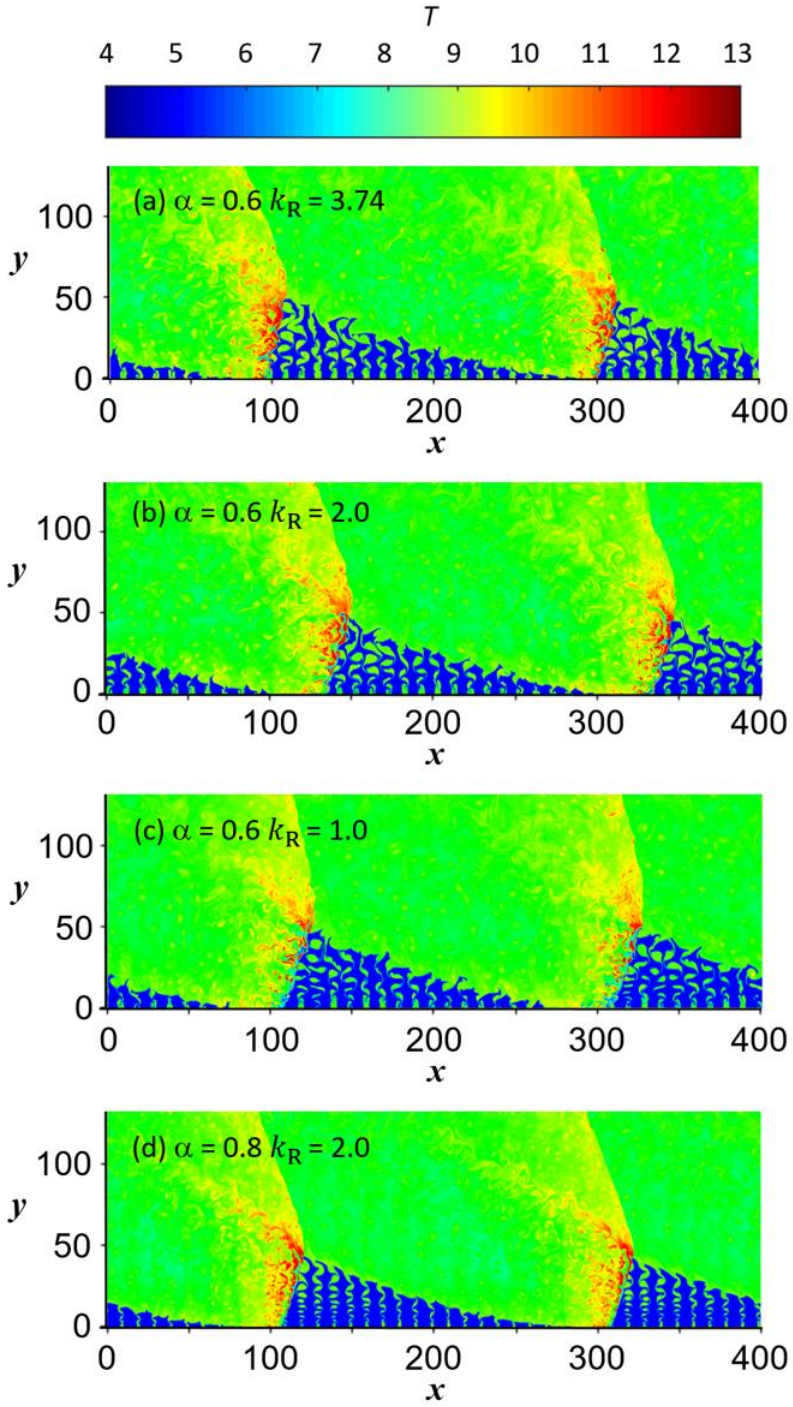

Figure 11. Temperature contour at T_{st} = 4.0 and fixed area ratio α = 0.6 with (a) k_R = 3.74; (b) k_R = 2.0; (c) k_R = 1.0; and fixed k_R = 2.0 with different area ratio (b) α = 0.6 and (d) α = 0.8

A salient difference between the slot nozzle and ideal micro-nozzle setup is that slot nozzle geometry introduces a source of flow disturbances. The intrinsic chemical instability and the inflow irregularity both affect the stability of the detonation wave front. As discussed in the previous section, a higher area ratio α leads to a less irregular inflow. For comparison, Fig. 11(d) shows the wavelet at α = 0.8 and k_R = 2.0. Comparing Fig. 11(d) with Fig. 11(b) at α = 0.6 and k_R = 2.0, the combustible jets are more regular and frequent and thus, a homogeneous reactant mixture is thus more apparent.

Figure 12 is the numerical soot foil of the RDWs in a single cycle. In numerical simulations, the maximum pressure in place is used to record the trajectory of the triple points in detonation front. These soot foils provide a visual representation of the chaotic magnitude of detonation wave instabilities. As shown in Fig 12(e), for the case with an ideal mini-nozzle injection and $k_R = 2.0$, the intrinsic cellular pattern of the resulting RDW is regular. For the cases with slot injection and $k_R = 2.0$, a decrease from $\alpha = 0.8$ to 0.6, as shown in Fig 12(d) and (b), respectively, the resulting cellular pattern becomes increasingly irregular. For the same injection area ratio $\alpha = 0.6$, a decrease in heat release rate controlled by the value of k_R, i.e., from $k_R = 3.74$ to 1.0 as shown in Fig. 12(a) to (c), respectively, the maximum pressure associated with the detonation-front triple points decreases.

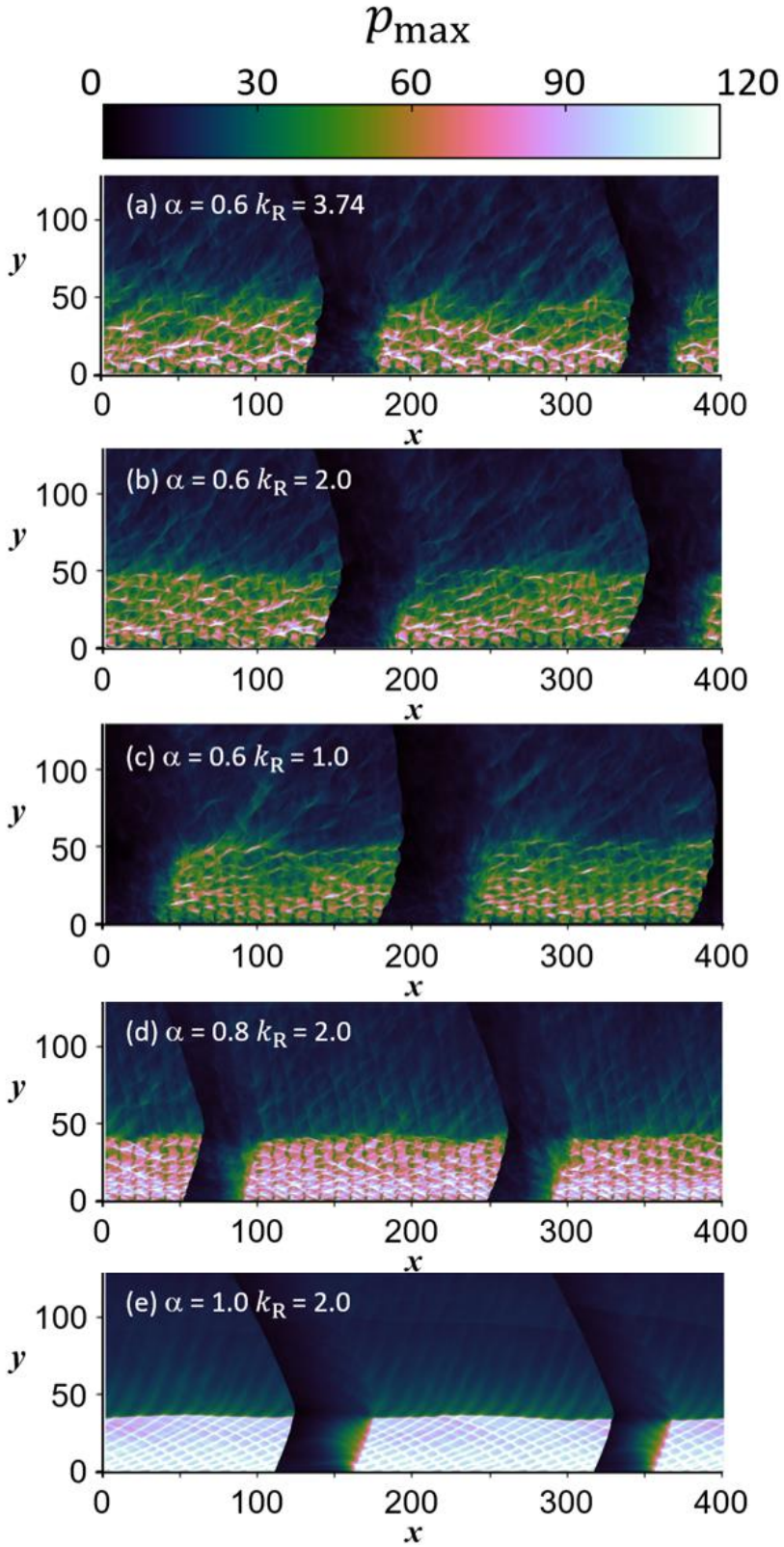

Figure 12. Numerical soot foil at T_{st} = 4.0, fixed area ratio α = 0.6 with (a) k_R = 3.74; (b) k_R = 2.0; (c) k_R = 1.0; and fixed k_R = 2.0 with different area ratio (b) α = 0.6, (d) α = 0.8 and (e) α = 1.0

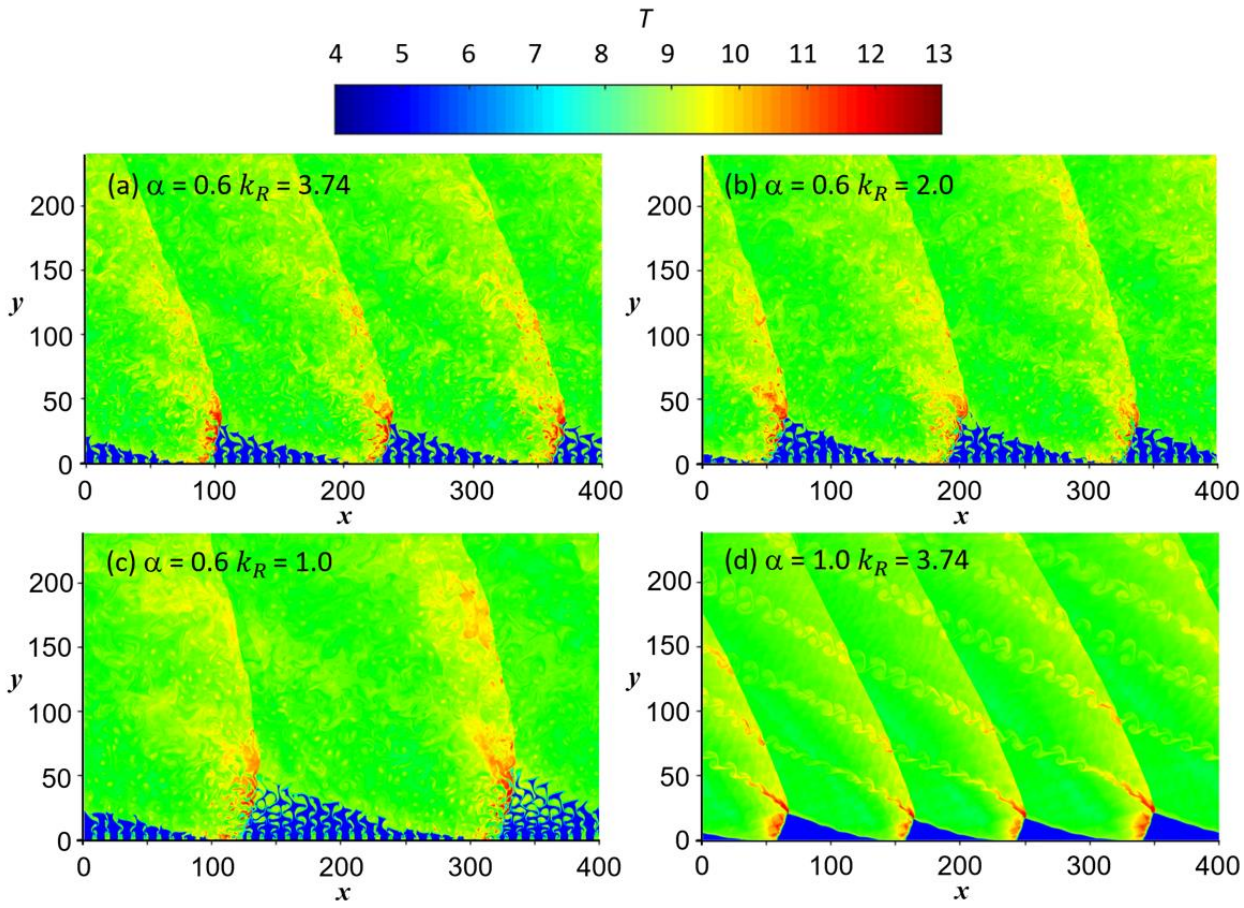

Figure 13. Temperature contour at T_{st} = 4.3 and fixed area ratio α = 0.6 with (a) k_R = 3.74; (b) k_R = 2.0; (c) k_R = 1.0; and fixed k_R=3.74 with different area ratio (a) α = 0.6 and (d) α = 1.0

The wavelet number is also quite insensitive to k_R. The k_R effect becomes more noticeable only at increasing T_{st} where a large number of wavelets could result. Figure 13 shows the results for T_{st} = 4.3 and α = 0.6 with decreasing k_R. A reduction in the wavelet number can be observed when k_R decreases to a small value k_R = 1.0. The resulting high wavelet number for the micro-nozzle at T_{st} = 4.3 is also included in Fig. 13 for comparison. Overall, it is thus suggested that parameters that affect the mass flow rate of the injection (e.g., slot area ratio α, T_{st}, etc.) play a more prominent role in determining the number of detonation wavelets in the given RDE. And in this simulation setup, for a low k_R value at k_R = 1.0, a quasi-steady state cannot be reached at the area ratio α = 0.8 and 1.0.

Table 4. The number of wavelets at $T_{st} = 4.3$ with different k_R and α

α \ k_R	**1.0**	**2.0**	**3.74**	**5.0**
0.6	2	3	3	3
0.8	-	3	3	3
1.0	-	2	4	3

5. Conclusions

Numerical simulations are carried out in this study to analyze two-dimensional RDWs with slot nozzle injection using the reactive Euler equations with two-step, induction-reaction chemical kinetics. The effects of plenum stagnation temperature, stagnation pressure, and heat release rate have been investigated based on the slot injection geometry with different nozzle area ratios, α. The simulation results demonstrate that these initial parameters have a similar influence on slot nozzle RDWs as compared with the mini-nozzle RDWs reported in the previous study [45]. Varying the slot nozzle throat area ratio, the present study, however, shows that the inhomogeneity imposed by spatially discrete injection slots plays a significant role on the resulting RDW propagation modes.

An increase in slot area ratio α has a stabilizing effect on RDWs. Due to the increase of total injection mass flow rate, the amount of burned gas that disturbs the inflow decreases, and thus, a greater amount of combustible gases is available to maintain a stable detonation wavefront. Consistent with the observation in the micro-nozzle case, a higher stagnation temperature leads to a higher number of detonation wavelets. RDWs are however prone to failure at a lower stagnation temperature in the slot nozzle case. Stagnation pressure does not directly influence the RDW pattern when it is sufficiently large to maintain the nozzles choked. A decrease in heat release rate

by decreasing the pre-exponential factor k_R leads to a reduced degree of instability of the detonation front and the fade-away of cellular detonation structure in mini-nozzle injection. In the slot nozzle injection, the spatial discreteness results in the irregularity of inflow taking the dominance of detonation surface instability.

Author Contributions

Conceptualization, H.T. and H.D.N.; methodology, C.Y..; Investigation, C.Y., H.T. and H.D.N.; writing—original draft preparation, C.Y. and H.D.N.; writing—review and editing, H.D.N.

Acknowledgment

This research is supported by the Natural Sciences and Engineering Research Council of Canada NSERC (No. RGPIN-2017-06698). The authors thank XiaoCheng Mi for comments and feedback on the manuscript.

Conflicts of Interest

The authors declare no conflict of interest.

References

1. Wolanski, P. Detonative propulsion. Proc. Combust. Inst. 2013, 34, 125–158.
2. Kailasanath, K. Review of propulsion applications of detonation waves. AIAA J. 2000, 38, 1698–1708.
3. Higgins, A.J. Ram accelerators: Outstanding issues and new directions. J. Propul. Power 2006, 22, 1170–1187.

4. Cambier, J.L.; Adelman, H.; Menees, G.P. Numerical simulations of an oblique detonation wave engine. J. Propul. 1990, 6, 315–323.
5. Roy, G.D.; Frolov, S.M.; Borisov, A.A.; Netzer, D.W. Pulse detonation propulsion: Challenges, current status, and future perspective. Prog. Energy Combust. Sci. 2004, 30, 545–672.
6. Smirnov, N.N.; Betelin, V.B.; Nikitin, V.F.; Phylippov, Yu. G.; Koo J. Detonation engine fed by acetylene–oxygen mixture. Acta Astronaut. 2014, 104, 134-146.
7. Lu, F.; Braun, E. Rotating detonation wave propulsion: Experimental challenges, modeling, and engine concepts. J. Prop. 2014, 30 (5), 1125–1142.
8. Zhou, R.; Wu, D.; Wang, J.P. Progress of continuously rotating detonation engines. Chin. J. Aero. 2016, 29(1), 15-29.
9. Kailasanath, K. Recent developments in the research on rotating-detonation-wave engines. In 55th AIAA aerospace sciences meeting, Texas, Grapevine, 2017, AIAA 2017-0784.
10. Rankin, B.A.; Fotia, M.L.; Naples, A.G.; Stevens, C.A.; Hoke, J.L.; Kaemming, T.A. et al. Overview of performance, application, and analysis of rotating detonation engine technologies. J Propul Power, 2017, 33, 131-143.
11. Bykovskii, F.A.; Zhdan, S.A. Current status of research of continuous detonation in fuel-air mixture (Review). Combust. Expl. Shock Waves 2015, 51, 21-35.
12. Hishida, M.; Fujiwara, T.; Wolanski, P. Fundamentals of rotating detonations. Shock Waves. 2009, 19, 1–10.
13. Ma, J.Z.; Luan, M.Y.; Xia, Z.J.; Wang, J.P.; Zhang, S.J.; Yao, S.B.; Wang, B. Recent progress, development trends, and consideration of continuous detonation engines. AIAA J. In press. https://doi.org/10.2514/1.J058157

14. Schwer, D.; Kailasanath, K. Fluid dynamics of rotating detonation engines with hydrogen and hydrocarbon fuels. Proc. Combust. Inst. 2013, 34, 1991–1998.
15. Schwer, D.; Kailasanath, K. Numerical investigation of the physics of rotating-detonation-engines. Proc. Combust. Inst. 2011, 33, 2195-2202.
16. Sun, J.; Zhou, J.; Liu, S.; Lin, Z. Numerical investigation of a rotating detonation engine under premixed/non-premixed conditions. Acta Astronaut. 2018, 152, 630-638.
17. Wang, Y.; Wang, J.P. Effect of equivalence ratio on the velocity of rotating detonation. Int. J. Hydrogen Energy 2015, 40(25), 7949-7955.
18. Schwer, D.A.; Kailasanath, K. Numerical study of the effects of engine size on rotating detonation engines. In: 49th AIAA aerospace sciences meeting, Orlando, FL 2011, AIAA 2011-581.
19. Tang, X.M.; Wang, J.P.; Shao, Y.T. Three-dimensional numerical investigations of the rotating detonation engine with a hollow combustor. Combust. Flame 2015, 162, 997–1008.
20. Katta, V.R.; Cho, K.Y.; Hoke, J.L.; Codoni, J.R.; Schauer, F.R.; Roquemore, W.M. Effect of increasing channel width on the structure of rotating detonation wave. Proc. Combust. Inst. 2019, 37, 3575-3583.
21. Zhao, M.; Li, J.M.; Teo, C.J.; Khoo, B.C.; Zhang, H.; Effects of variable total pressures on instability and extinction of rotating detonation combustion. Flow, Turbul. Combust. 2020, 104, 261-290.
22. Yamada, T.; Hayashi, A.K.; Yamada, E.; Tsuboi, N.; Tangirala, V.E.; Fujiwara, T. Detonation limit thresholds in H2/O2 rotating detonation engine. Combust. Sci. Technol. 2020, 182, 1901–1914.

23. Meng, Q., Zhao, N., Zheng, H., Yang, J.: Numerical investigation of the effect of inlet mass flow rates on H2/air non-premixed rotating detonation wave. Int. J. Hydrog. Energy. 43, 13618–13631 (2018)
24. Yao, S.Z.S., Zhang, M.L.L.: Effects of injection conditions on the stability of rotating detonation waves.
Shock Waves. 28, 1079–1087 (2018)
25. Anand, V.; St George, A.; Driscoll, R.; Gutmark, E.; Characterization of instabilities in a rotating detonation combustor. Int. J. Hydrogen Energy 2015, 40, 16649-16659.
26. Anand, V.; Gutmark, E. Rotating detonation combustors and their similarities to rocket instabilities. Prog. Energy Combust. Sci. 2019, 73, 182-234.
27. Anand, V.; St George, A.; Driscoll, R.; Gutmark, E.; Longitudinal pulsed detonation instability in a rotating detonation combustor. Exp. Therm. Fluid Sci. 2016, 77, 212-225.
28. Liu, Y.; Zhou, W.; Yang, Y.; Liu, Z.; Wang, J.; Liu, Y.; Zhou, W.; Yang, Y.; Liu, Z.; Wang, J. Numerical study on the instabilities in H2-air rotating detonation engines numerical study on the instabilities in H2-air rotating detonation engines. Phys. Fluids 2018, 046106.
29. Liu, Y., Chen, Y.L., Xia, Z.J., Wang, J.P. Numerical study of the reverse-rotating waves in rotating detonation engine with a hollow combustor. Acta Astronaut. 2020, 170, 421-430.
30. Zhang, S.; Yao, S.; Luan, M.; Zhang, L.; Wang, J. Effects of injection conditions on the stability of rotating detonation waves. Shock Waves 2018, 28, 1079-1087.
31. Smirnov, N.N.; Nikitin, V.F.; Stamov, L.I.; Mikhalchenko, E.V.; Tyurenkova, V.V. Three-dimensional modeling of rotating detonation in a ramjet engine. Acta Astronaut. 2019, 163, 168-176.

32. Smirnov N.N.; Nikitin V.F.; Stamov L.I.; Mikhalchenko E.V.; Tyurenkova V.V. Rotating detonation in a ramjet engine three-dimensional modeling. Aero. Sci. Tech. 2018, 81, 213-224.
33. Deng, L.; Ma, H.; Xu, C.; Zhou, C.S.; Liu, X. Investigation on the propagation process of rotating detonation wave. Acta Astronaut. 2017, 139, 278-287.
34. Jourdaine, N.; Tsuboi, N.; Ozawa, K.; Kojima, T.; Koichi Hayashi, A. Three-dimensional numerical thrust performance analysis of hydrogen fuel mixture rotating detonation engine with aerospike nozzle. Proc. Combust. Inst. 2018, 37(3), 3443–3451
35. Braun, J.; Saracoglu, B.H.; Paniagua, G. Unsteady performance of rotating detonation engines with different exhaust nozzles. J. Propuls. Power. 33, 121–130 (2017)
36. Shao, Y.T.; Liu, M.; Wang, J.P. Numerical investigation of rotating detonation engine propulsive performance. Combust. Sci. Technol. 182, 1586–1597 (2010)
37. Shao, Y.; Liu, M.; Wang, J. Continuous detonation engine and effects of different types of nozzle on its propulsion performance. Chinese J. Aeronaut. 23, 647–652 (2010)
38. Yi, T.-H.; Lou, J.; Turangan, C.; Choi, J.-Y.; Wolanski, P. Propulsive performance of a continuously rotating detonation engine. J. Propuls. Power. 27, 171–181 (2011)
39. Yokoo, R.; Goto, K.; Kim, J.; Kawasaki, A.; Matsuoka, K.; Kasahara, J.; Matsuo, A.; Funaki, I. Propulsion Performance of Cylindrical Rotating Detonation Engine. AIAA J. https://doi.org/10.2514/1.J058322
40. Tsuboi, N.; Watanabe, Y.; Kojima,T.; Hayashi, A.K. Numerical estimation of the thrust performance on a rotating detonation engine for a hydrogen-oxygen mixture. Proc. Combust. Inst. 2015, 35, 2005-2013.

41. Betelin, V.B.; Nikitin, V.F.; Mikhalchenko, E.V. 3D numerical modeling of a cylindrical RDE with an inner body extending out of the nozzle. Acta Astronaut. 176, 2020, 628-646.
42. Schwer, D.; Kailasanath, K. Effect of inlet on fill region and performance of rotating detonation engines. 47th AIAA/ASME/SAE/ASEE Joint Propulsion Conference & Exhibit, 31 July-03 August, 2011, San Diego CA.
43. Sun, J.; Zhou, J.; Liu, S.; Lin, Z.; Cai, J. Effects of injection nozzle exit width on rotating detonation engine. Acta Astronaut. 2017, 140, 388–401.
44. Palaniswamy, S.; Akdag, V.; Peroomian, O.; Chakravarthy, S. Comparison between ideal and slot injection in a rotating detonation engine. Combust. Sci. Technol. 2018, 190, 557–578.
45. Teng, H.; Zhou, L.; Yang, P.F.; Jiang, Z.L. Numerical investigation of wavelet features in rotating detonations with a two-step induction-reaction model. Int. J. Hydrogen Energy 2020, 45, 4991-5001.
46. Ng, H.D.; Radulescu, M.I.; Higgins, A.J.; Nikiforakis, N.; Lee, J.H.S. Numerical investigation of the instability for one-dimensional Chapman–Jouguet detonations with chain-branching kinetics. Combust. Theory Modell. 2005, 9, 385–401.
47. Yang, P.F.; Teng, H.H.; Jiang, Z.L.; Ng, H.D. Effects of inflow Mach number on oblique detonation initiation with a two-step induction-reaction kinetic model. Combust. Flame 2018, 193, 246–256.
48. Tang-Yuk, K.C.; Mi, X.C.; Lee, J.H.S.; Ng, H.D. Transmission of a detonation across a density interface. Shock Waves 2018, 28, 967–979.
49. Li, J.; Ning, J. Experimental and numerical studies on detonation reflections over cylindrical convex surfaces. Combust. Flame 2018, 198, 130–145.

50. Xiang, G.X.; Gao, X.; Tang, W.J.; Jie, X.Z.; Huang, X. Numerical study on transition structures of oblique detonations with expansion wave from finite-length cowl. Phys. Fluids 2020, 32, 056108.
51. Yuan, X.Q.; Zhou, J.; Mi, X.C.; Ng, H.D. Numerical study of cellular detonation wave reflection over a cylindrical concave wedge. Combust. Flame 2019, 202, 179-194.
52. Yan, C.; Teng, H.H.; Mi, X.C.; Ng, H.D. The effect of chemical reactivity on the formation of gaseous oblique detonation waves. Aerospace (MDPI) 2019, 6, 62.
53. Toro, E.F. Riemann Solvers and Numerical Methods for Fluid Dynamics, 3rd ed.; Springer: Berlin, Germany, 2009.
54. Kiyanda, C.B.; Morgan, G.H.; Nikiforakis, N.; Ng, H.D. High resolution GPU-based flow simulation of the gaseous methane-oxygen detonation structure. J. Vis. 2015, 18, 273–276.
55. Mi, X.C.; Higgins, A.J.; Ng, H.D.; Kiyanda, C.B.; Nikiforakis, N. Propagation of gaseous detonation waves in a spatially inhomogeneous reactive medium. Phys. Rev. Fluids 2017, 2, 053201.
56. Mi, X.C.; Higgins, A.J.; Kiyanda, C.B.; Ng, H.D.; Nikiforakis, N. Effect of spatial inhomogeneities on detonation propagation with yielding confinement. Shock Waves 2018, 28, 993–1009.
57. Uemura, Y.; Hayashi, A.K.; Asahara, M.; Tsuboi, N.; Yamada, E. Transverse wave generation mechanism in a rotating detonation. Proc. Combust. Inst. 2013, 34(2), 1981-1989.
58. Smirnov, N.N.; Betelin, V.B.; Nikitin, V.F.; Stamov, L.I.; Altoukhov, D.I. Accumulation of errors in numerical simulations of chemically reacting gas dynamics. Acta Astronaut. 2015, 117, 338–355.

59. Smirnov, N.N.; Betelin, V.B.; Shagaliev, R.M.; Nikitin, V.F.; Belyakov, I.M.; Deryuguin, Yu.N.; Aksenov, S.V.; Korchazhkin, D.A. Hydrogen fuel rocket engines simulation using LOGOS code. Int. J. Hydrog. Energy 2014, 39(20), 10748–10756.
60. Ng, H.D.; Zhang, F. Detonation Instability. In Shock Wave Science and Technology Library; Zhang, F., Ed.; Springer: Berlin, Germany, 2012; Volume 6, Chap. 3.

List of figures

Figure 13. Temperature contour at T_{st} = 4.3 and fixed area ratio α = 0.6 with (a) k_R = 3.74; (b) k_R = 2.0; (c) k_R = 1.0; and fixed k_R=3.74 with different area ratio (a) α = 0.6 and (d) α = 0.8

List of tables

Effects of Slot Injection on Detonation Wavelet Characteristics in a Rotating Detonation Engine

Chian Yan [1*], Honghui Teng [2] and Hoi Dick Ng [1]

[1] Department of Mechanical, Industrial and Aerospace Engineering, Concordia University, Montreal, QC H3G 1M8, Canada
[2] School of Aerospace Engineering, Beijing Institute of Technology, Beijing 100081, China

*** Correspondence:** chian.yan@concordia.ca

Declaration of interests

☒ The authors declare that they have no known competing financial interests or personal relationships that could have appeared to influence the work reported in this paper.

☐The authors declare the following financial interests/personal relationships which may be considered as potential competing interests: